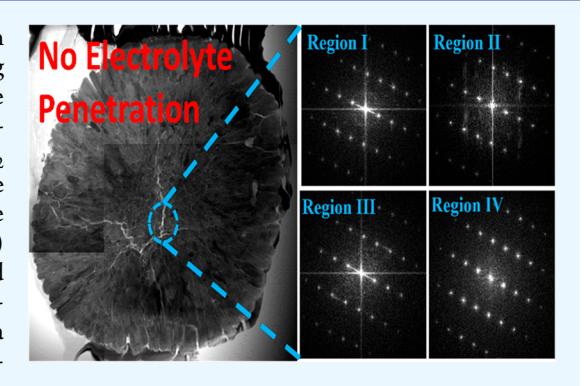
Nanorod Gradient Cathode: Preventing Electrolyte Penetration into **Cathode Particles**

Ho-Hyun Sun,[†] Jason A. Weeks,[‡] Adam Heller,[†] and C. Buddie Mullins*,[†],[‡]

[†]McKetta Department of Chemical Engineering and [‡]Department of Chemistry, The University of Texas at Austin, Austin, Texas 78712, United States

Supporting Information

ABSTRACT: Layered nickel-rich cathode particles for lithium-ion batteries can fail and severely limit the cycling performance via cracking from anisotropic strain which allows electrolyte penetration and the formation of electrically insulating material and a decreased capacity. Selfassembled layered nanorod gradient (NRG) Li[Ni_{0.81}Co_{0.06}Mn_{0.13}]O₂ cathode particles cycle more stably with improved performance compared to its constant concentration counterpart. NRG cathode material was synthesized with a Ni-rich bulk (for higher lithium storage) and a radially columnar nanorod comprised surface and benchmarked against the widely used constant concentration (CC) LI[Ni_{0.82}-Co_{0.14}Al_{0.04}]O₂ cathode and in both half- and full-cells. Through a combination of in situ and time-resolved X-ray diffraction (XRD), crosssection scanning electron microscopy imaging (SEM), and high-



resolution transmission electron microscopy (HR-TEM), we confirm that the enhanced durability of the NRG material is attributed to its radially columnar concentration graded nanorods at the surface. These nanorods function as a buffer to diminish abrupt stress from the high Ni-content bulk during the H2 → H3 phase transition by suppressing crack propagation to preserve particle coherency, enabling reversibility of the cathode particle. Notably, we show that electrolyte infiltration into the reactive Ni-rich bulk and subsequent formation of the electrically insulating rock-salt nanostructure (NiO) along the cracks are prevented, thereby minimizing impedance increase during long-term cycling. Furthermore, the increased Mn concentration at the outer surface of the nanorods also enhances the thermal stability by delaying the layered to rock-salt phase transition on the surface.

KEYWORDS: Ni-rich layered oxide cathode, gradient cathode, Li-ion batteries, in situ XRD, particle cross section, HR-TEM

1. INTRODUCTION

More than two and a half decades have passed since the introduction of LiCoO2 as the first commercial Li-ion battery cathode. Since then, Li-ion batteries (LIBs) have made great progress and become an essential energy storage device in our society. Recently, they have started to be employed as main energy providers in larger applications such as electric vehicles (EVs) and energy storage systems (ESSs) which require higher energy density and longer cycle life. To suit the needs of these complex systems, numerous cathode 1-5 and anode 6-8 materials have been explored. But because of the lower capacity and cycling performance of cathodes compared to anodes, cathodes have been the bottleneck for battery performance.

Among the cathode materials, layered transition metal oxides (LiTMO₂, TM = transition metals) are seen as strong contenders due to their high gravimetric and volumetric energy densities; Li[Ni_xCo_vMn_z]O₂ (NCM)⁹⁻¹¹ and Li[Ni_xCo_vAl_z]O₂ (NCA)^{10,12,13} are already being used in the Chevy Volt, Nissan Leaf, and Tesla Model S and X. Nonetheless, a growing demand for higher energy densities calls for even higher practical capacities, and the U.S. Department of Energy (DOE)

has estimated that to guarantee the success of EVs, a driving range of at least 300 miles, 14 translating to 350 Wh kg $^{-1}$ at the cell level and 800 Wh kg $^{-1}$ (216 mAh g $^{-1}$ at 3.7 V) at the cathode active material level, is required. This can be achieved by increasing the Ni concentration in NCM and NCA but is accompanied by a loss in structural and chemical stabilities, especially above 80% Ni content 15,16 as Ni-rich NCM suffers from surface deterioration from the Ni redox reaction to $\mbox{Ni}^{2+\,17-20}$ and bulk degradation from crack generation caused by the repeated stress during the H2 -> H3 phase transition. 21-24

Numerous attempts have been made to realize both high capacity and stability of NCM materials through mitigation of the impact of such degradation mechanisms. Transition metal compositions have been varied to identify the most optimal performance composition. 11,15,16 Structural integrity has been improved by doping the particle bulk with Fe, Mg, Al, Zn, Ti, B, Zr, and W. ^{19,25-30} Surface chemical stability has been

Received: June 5, 2019 Accepted: July 12, 2019 Published: July 12, 2019

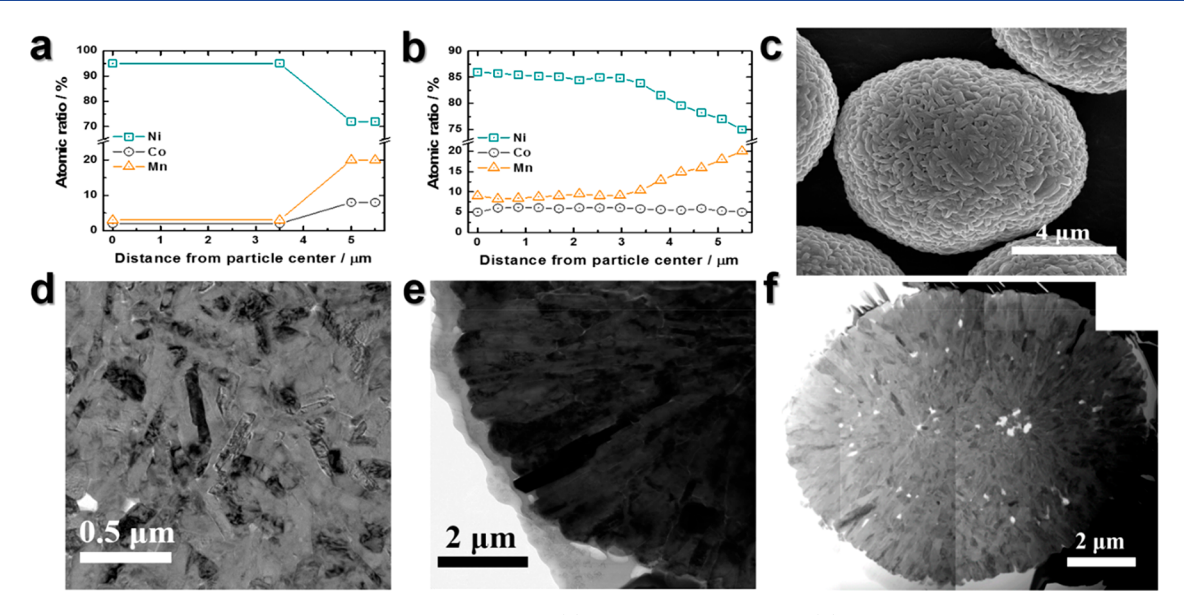


Figure 1. NRG81 Li[Ni_{0.81}Co_{0.06}Mn_{0.13}]O₂ oxide Ni, Co, and Mn (a) design concentrations, (b) lithiated oxide concentrations, and (c) SEM image of the NRG81 cathode particle. TEM image of cross-sectioned NRG81 particle (d) bulk region, (e) graded nanorod shell region, and (f) whole particle.

improved by coating with a layer of Al_2O_3 , AlF_3 , $Al(OH)_3$, ZrO_2 , and C nanolayers.^{31–35} However, composition variations are inherently limited by the capacity versus stability trade-off, and both doping and coating processes add inactive materials into the electrode, thereby lowering the energy density. In a different approach, Sun et al. 36-41 created materials with a concentration gradient in which the Mn-rich surface shields the Ni-rich bulk to allow both high capacity and stable cycling. More practically, it also uses the same conventional cathode material synthesis process and can readily be integrated into existing cathode manufacturing process. Nevertheless, the Mnrich shell lowers the total Ni content in the cathode and further necessitates a highly Ni-rich bulk to balance the Ni decrease in the shell. Unfortunately, the increased Ni content bulk acts similarly to $\text{LiNiO}_2^{19,21,23,41}$ and the intensified H2 \rightarrow H3 phase transition strains the overall cathode structure.

Recently, the same group has proposed a new degradation mechanism¹⁶ in which (i) electrolyte penetrates cathode particles via interparticle crack networks reaching the surface and (ii) the subsequent formation of a rock-salt impurity phase (NiO) along the cracks greatly increases electrical resistance. These factors are cited as the main source of capacity fade for conventional Ni-rich NCMs. In this paper, we investigate whether the same degradation mechanism holds true for a radially columnar concentration graded nanorod cathode. Through a systematic comparison of the nanorod gradient Li[Ni_{0.81}Co_{0.06}Mn_{.0.13}]O₂ (hereafter denoted as NRG81) to the prominent constant composition Li[Ni_{0.82}Co_{0.14}Al_{0.04}]O₂ (hereafter as CC82) under strenuous conditions of substantially increased total Ni content in both the bulk and nanorods and raised cutoff voltage of 4.4 V, we explore the factors that distinguish the nanorod material from conventional cathodes in pouch-type full-cells cycled up to 1000 cycles in its electrochemical performance and electrolyte penetration prevention. A combination of in situ and time-resolved (TR)-XRD, particle cross-section SEM images, and highresolution TEM (HR-TEM) analysis is used to examine the micro- and nanostructure of the cycled cathodes and their effect on electrolyte penetration prevention into the Ni-rich

core. On the basis of these analyses, we address the need for a stable high energy (\geq 800 Wh kg $^{-1}$) density cathode through the nanorod gradient design from both a micro- and nanostructure perspective.

2. EXPERIMENTAL SECTION

2.1. Synthesis of Nanorod Gradient Li[Ni_{0.81}Co_{0.06}Mn_{.0.13}]O₂ **Cathode.** The nanorod gradient Li[Ni_{0.81}Co_{0.06}Mn_{.0.13}]O₂ cathode was synthesized by a hydroxide coprecipitation method as reported in the literature. 9,36 NiSO₄·6H₂O, CoSO₄·7H₂O, and MnSO₄·5H₂O (95:2:3 molar ratio) were initially fed into a 14 L stirred tank reactor to create a highly Ni-rich core [Ni_{0.95}Co_{0.02}Mn_{0.03}](OH)₂. A less Nirich solution (Ni:Co:Mn = 0.72:0.08:0.20) was simultaneously pumped into the highly Ni-rich solution tank after a certain period of time to achieve the gradient between the bulk and shell. The resulting hydroxide particles were filtered, washed, and vacuum-dried at 110 °C. Afterward, the dried hydroxides were mixed with LiOH in a 1:1 molar ratio and calcined at 770 °C for 10 h under a high-purity oxygen atmosphere. The Li[Ni $_{0.82}$ Co $_{0.14}$ Al $_{0.04}$]O $_2$ was purchased from EcoPro (Seoul, Republic of Korea).

2.2. Cathodes and Electrochemical Testing. The synthesized bulk-shell rod-gradient Li[Ni_{0.81}Co_{0.06}Mn_{0.13}]O₂ and EcoPro constant concentration $Li[Ni_{0.82}Co_{0.14}Al_{0.04}]O_2$ powders were mixed with carbon black and poly(vinylidene fluoride) (PVDF) in a 90:5.5:4.5 wt % ratio in N-methyl-2-pyrrolidone (NMP) and cast onto Al foil. Afterward, the cast electrodes were vacuum-dried at 110 °C and rollpressed to result in an active material loading of ~6 mg cm⁻². Electrodes were punched out and assembled in 2032 coin-type halfcells with Li metal as an anode and 1.2 M LiPF₆ in ethylene carbonate (EC):ethyl methyl carbonate (EMC) = 3:7 vol % with 2 wt % vinylene carbonate (VC) as electrolyte. Pouch-type full-cells were assembled for long-term cycling with the bulk-shell rod-gradient $Li[Ni_{0.81}Co_{0.06}Mn_{0.13}]O_2$ and EcoPro constant concentration Li- $[\mathrm{Ni}_{0.82}\mathrm{Co}_{0.14}\mathrm{Al}_{0.04}]\mathrm{O}_2$ as cathodes and graphite as an anode. The half-cells were cycled between 2.8 and 4.4 V at 0.5 C and 30 °C, and full-cells were cycled between 2.8 and 4.3 V at 1.0 C and 25 °C.

2.3. Instruments and Software. Inductively coupled plasma atomic emission spectroscopy (ICP-AES) (OPIMA8300, PerkinElmer) was used to determine the chemical compositions of the synthesized powders. Powder X-ray diffraction (XRD) (Rint-2000, Rigaku) was employed to measure the crystalline structure of the powders and measured with Cu K α radiation from $2\theta = 10^{\circ}$ to 110° with a step size of 0.02°, and lattice parameters were obtained by

Rietveld refinement employing the FullProf software package. Particle morphologies were observed by using scanning electron microscopy (SEM) (JSM-6340F, JEOL), and cross sections of the particles were obtained by using a focused ion beam (FIB) (NOVA 200/FEI). In situ XRD (Malvern Panalytical Empyrean, Rigaku) was performed with a modified pouch-type half-cell with a beryllium-covered 5.0 mm diameter hole at its center for the X-ray beam path. In situ XRD data were taken every 3.5 min while the cell was being cycled with a constant current of 18 mA g⁻¹. Time-resolved XRD (TR-XRD) (R-AXIS IV++, Rigaku) was used to analyze the thermal properties of the cathodes by using pouch-type half-cells fabricated with bulk-shell rodgradient Li[Ni $_{0.81}$ Co $_{0.06}$ Mn $_{0.13}$]O $_{2}$ and EcoPro constant concentration $\text{Li}[\text{Ni}_{0.82}\text{Co}_{0.14}\text{Al}_{0.04}]O_2$ as cathodes and lithium metal as the anode. The half-cells were charged at a C/10 rate to a level corresponding to a composition of Li_{0.16}[Ni_{0.81}Co_{0.06}Mn_{0.13}]O₂ and Li_{0.16}[Ni_{0.82}Co_{0.14}Al_{0.04}]O₂, under the assumption that all the current passed through was used to extract lithium. The electrically delithiated cathodes were scraped from the aluminum current collector and sealed completely and mounted on the thermal stage of the TR-XRD system. Confirmation of the transition metal concentrations was confirmed via an electron probe microanalyzer (EPMA) (JXA-8100, JEOL). Transmission electron microscopy (TEM) (JEM2010, JEOL) was used to observe the structure damage of the recovered aftercycled electrodes.

3. RESULTS AND DISCUSSION

3.1. Cathode Chemical Composition and Crystal **Chemistry.** Our NRG81 particles were designed (Figure 1a) to have an almost pure Ni core (~95% Ni, 2% Co, and 3% Mn) for high capacity and a Mn-rich surface (~72% Ni, 8% Co, 20% Mn) for cycling stability with a concentration gradient in-between to alleviate anisotropic lattice expansion variations arising from composition differences. 43 The coprecipitated hydroxide precursor to the NRG81 particles was spherical and had identical transition metal concentrations as originally designed (Figure S1a,b). However, under hightemperature calcination conditions, the metal concentrations changed slightly due to atomic interdiffusion to result in a highly Ni-rich core (~86% Ni, 5.0% Co, and 9% Mn) which graded to a Mn-rich shell (~75% Ni, 5.0% Co, and 20% Mn) (Figure 1b) to achieve an overall chemical composition of $\text{Li}[\text{Ni}_{0.81}\text{Co}_{0.06}\text{Mn}_{0.13}]\text{O}_2$ determined by inductively coupled plasma atomic emission spectroscopy (ICP-AES). The constant concentration Li[Ni_{0.82}Co_{0.14}Al_{0.04}]O₂ (CC82) was purchased from EcoPro. 42 Both NRG81 and CC82 were spherical with a size of $\sim 10 \, \mu \text{m}$ and composed of smaller bulky primary particles (Figure 1c and Figure S1c). However, unlike the constant concentration CC82, which is composed of randomly oriented polygonal primary particles as shown previously in the literature, 16 NRG81 is composed of two distinct regions: the graded nanorod outer shell and constant concentration core. Like the CC82, the bulk was formed from arbitrarily oriented primary particles (Figure 1d), but the graded nanorod shell region was composed of radially elongated rods (Figure 1e). Rietveld refinement of the asprepared XRD patterns, seen in Figure S1d,e, showed that the oxides possessed distinct O3 type α-NaFeO₂ layered crystal structures in the Rm space group with crystal lattices of a =2.876(1) Å and c = 14.214(2) Å $(R_{wp} = 9.76)$ for NRG81 and a = 2.865(1) Å and c = 14.181(2) Å $(R_{wp} = 8.36)$ for CC82, matching those of previously reported results. 16 Cation mixing of $\text{Li}^+/\text{Ni}^{2+}$ for the NRG81 and CC82 was 3.212% and 2.740%, respectively.

3.2. Fundamental Electrochemical Performance. Figure 2 shows the fundamental electrochemical performance

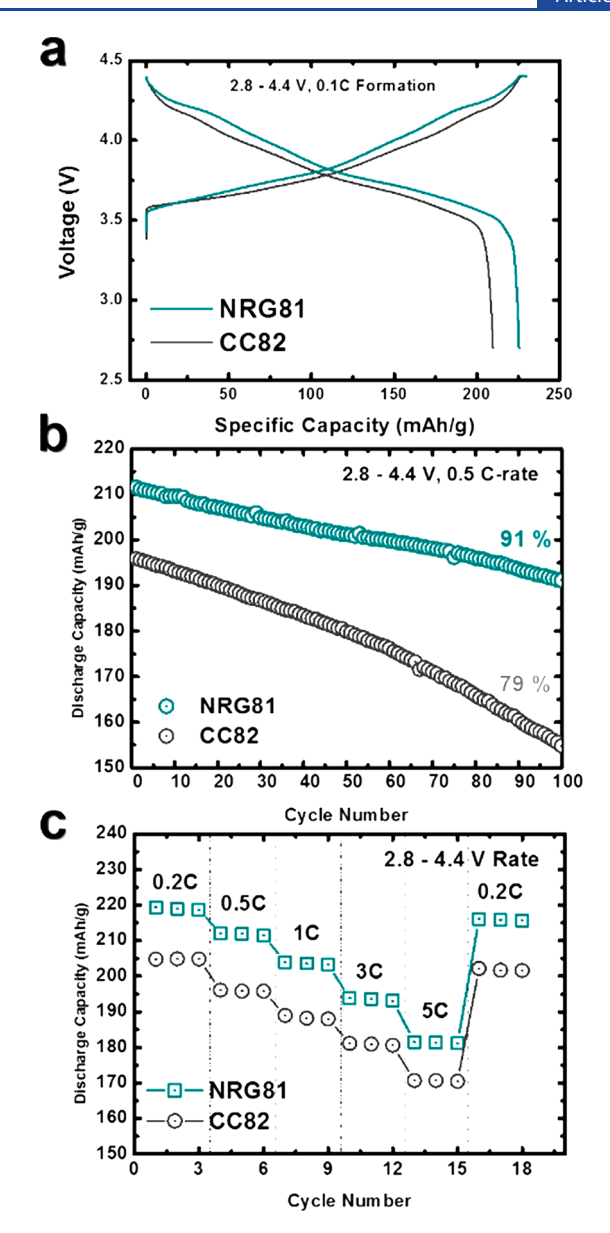


Figure 2. Fundamental electrochemical performance of NRG81 vs CC82 in half-cells: (a) 0.1 C first charge–discharge profiles, (b) cycle performance, and (c) rate capability.

of NRG81 and CC82 half-cells cycled between 2.8 and 4.4 V at 0.5 C (90 mA g⁻¹). During the first cycle, NRG81 and CC82 discharged up to 225 and 210 mAh g⁻¹ with Coulombic efficiencies of 95.7% and 92.4% at 0.1 C, respectively (Figure 2a). The NRG81 cathode retained 91% of its discharge capacity following 100 cycles while the CC82 cathode retained only 79%. Interestingly, despite having similar nickel compositions and less than half the amount of cobalt, NRG82 exhibited higher discharge capacities at all C-rates, even at the faster rates of 3 and 5 C (Figure 2c and Table S1). The high capacity is attributed to the rodlike primary particles in the shell region being radially aligned parallel to Licontaining crystal planes, which enhances the transport of Li⁺.18,39-41 As such, the NRG81 outperforms its constant concentration counterpart and is composed of lower cost materials.

3.3. Long-Term Full-Cell Performance. The difference in electrochemical performance of NRG81 and CC82 is further

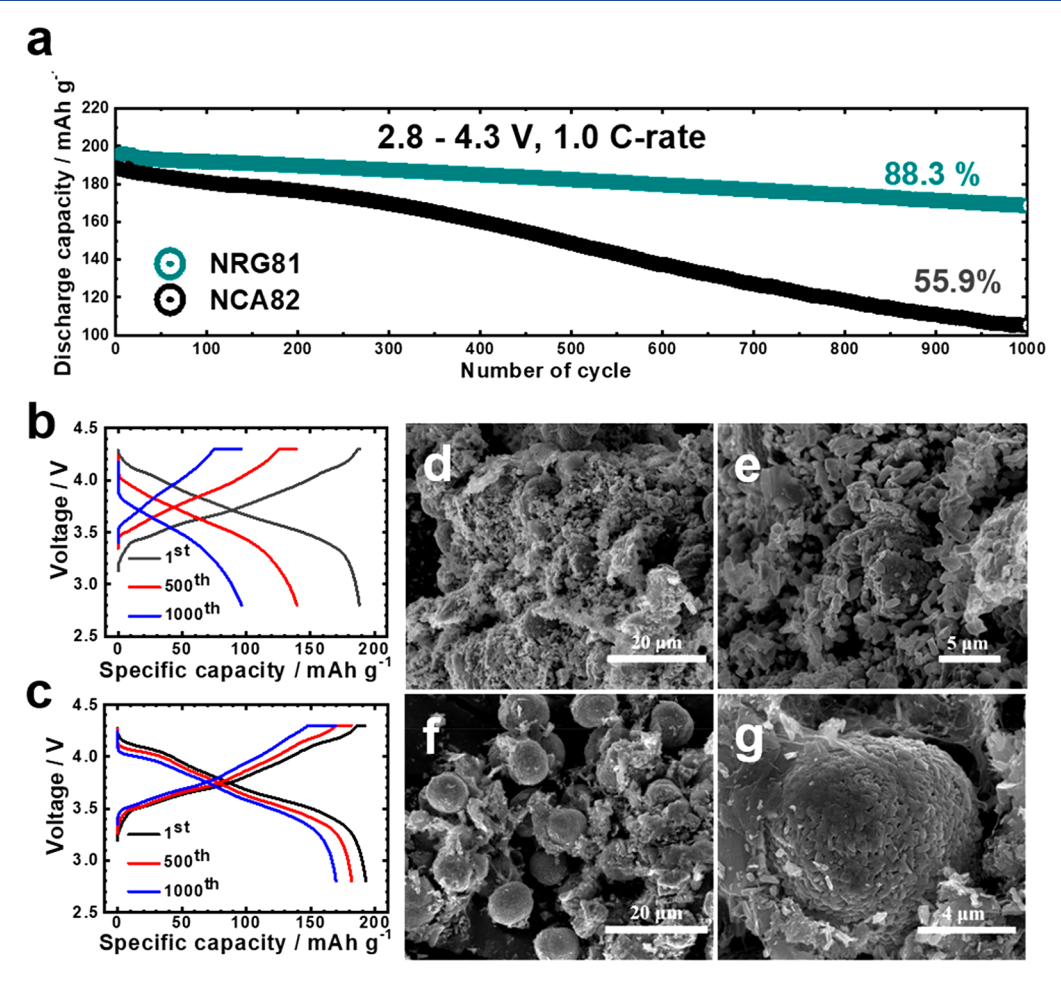


Figure 3. Comparison of long-term cycling (1000 cycles) performances of NRG81 vs CC82 in pouch-type full-cells: (a) 1.0 C-rate cycling performance and corresponding (b) CC82 charge—discharge curves and (c) NRG81 charge—discharge curves. Post-mortem electrode particle SEM images of (d, e) CC82 and (f, g) NRG81.

amplified in pouch-type full-cells (cathodes: NRG81 and CC82; anode: graphite) cycled for 1000 cycles as seen in Figure 3. As in the case of half-cells, NRG81 delivered a higher first discharge capacity of 195 mAh g⁻¹ compared to 188 mAh g^{-1} for CC82 at 1.0 C and 2.8-4.3 V. Up to 1000 cycles, NRG81 exhibited stable consecutive discharge capacities to result in a capacity retention of 88.3%. In contrast, the CC82 discharge capacity started to deteriorate beginning with its 300th cycle to the final 55.9% retention rate, losing almost half of its original discharge capacity. Correspondingly, the NRG81 full-cell better retained its charge-discharge curves than the CC82 full-cell which suffered from both severe capacity and voltage fade with progressive cycles (Figure 3b,c). The significantly higher long-term capacity retention of NRG81 is corroborated by SEM images of cathode particles recovered from the post-mortem full-cells (Figure 3d,e) which reveal that NRG81 particles maintain their original morphology and remained intact, whereas CC82 particles completely disintegrate to their individual primary particles. However, just the outward superficial appearance does not fully explain the superior cycling performance of NRG81.

3.4. Microstructure Cohesion. Previous reports by Sun et al. have referred to the $H2 \rightarrow H3$ phase transformation and abrupt volume change, 16,23 accompanied by electrolyte penetration through interparticle cracks, as the major culprit of capacity fade in Ni-rich layered cathodes. To quantitatively

ascertain the extent of the H2 \rightarrow H3 phase transformation, in situ XRD was taken on pouch-type half-cells (cathode: NRG81 and CC82; anode: lithium metal) during their 1st and 20th charge-discharge at a constant current density of 18 mA g⁻¹ up to 4.4 V. From the XRD contour plots in Figure S2, the (110) peak continuously shifts to higher angles, but the (003) peak shifts initially to lower angles and shifts back to higher angles by the end of charging for both NRG81 and CC82. The opposite is true in discharge. Reflecting the XRD peak shifts, the Rietveld refined a-axis lattice parameter values of NRG81 and CC82 contract continuously to result in similar parameter changes of $\Delta a = -2.05\%$ and $\Delta a = -2.08\%$, respectively, during the first charge while the c-axis values increase to reach a maximum at \sim 4.0 V (Li_{NRG} = 0.422, Li_{CC} = 0.416) and dramatically decrease to result in $\Delta c = -3.47\%$ and $\Delta c =$ -3.56% (Figure 4a,b). The resulting volume changes of NRG81 and CC82 during the first cycle are $\Delta V = -6.0\%$ for the former and $\Delta V = -5.38\%$ for the latter with significantly an accelerated ΔV occurring after introduction of the H2 \rightarrow H3 phase transition. Note that the larger ΔV of NRG81 can be attributed to NRG81 extracting more lithium ($Li_{NRG} = 0.145$, Li_{CC} = 0.183), which in turn results in the nanorod gradient material delivering the higher discharge capacity shown in

Indeed, the abrupt volume change of the $H2 \rightarrow H3$ phase transition severely affects the cathode microstructure. To

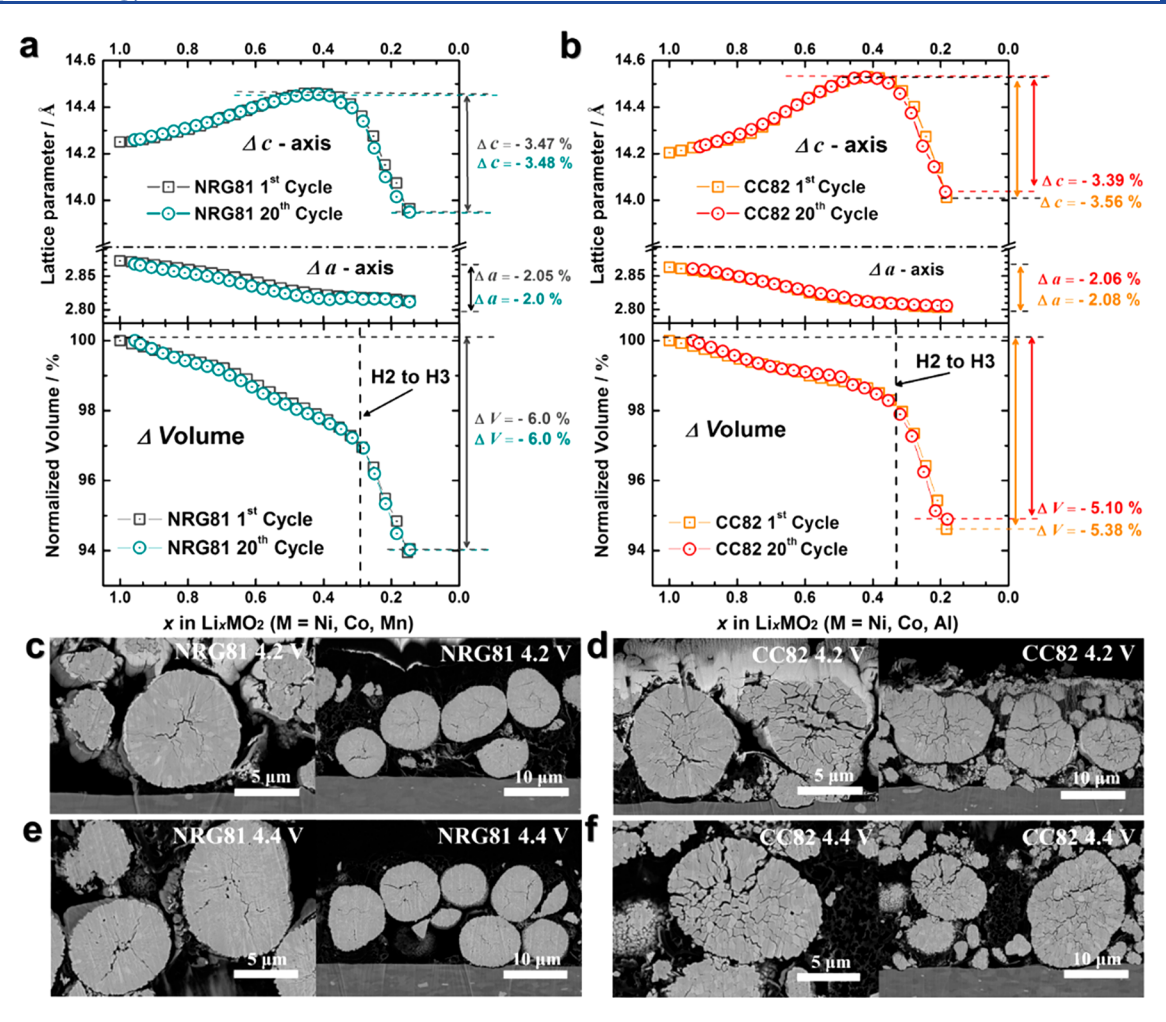


Figure 4. In situ XRD Rietveld refined a- and c-axis lattice and volume parameters of (a) NRG81 and (b) CC82 from 2.8 to 4.4 V. Cross-sectioned SEM images of (c) NRG81 and (d) CC82 at 4.2 V 1st cycle charged state and (e) NRG81 and (f) CC82 at 4.4 V 1st charged state.

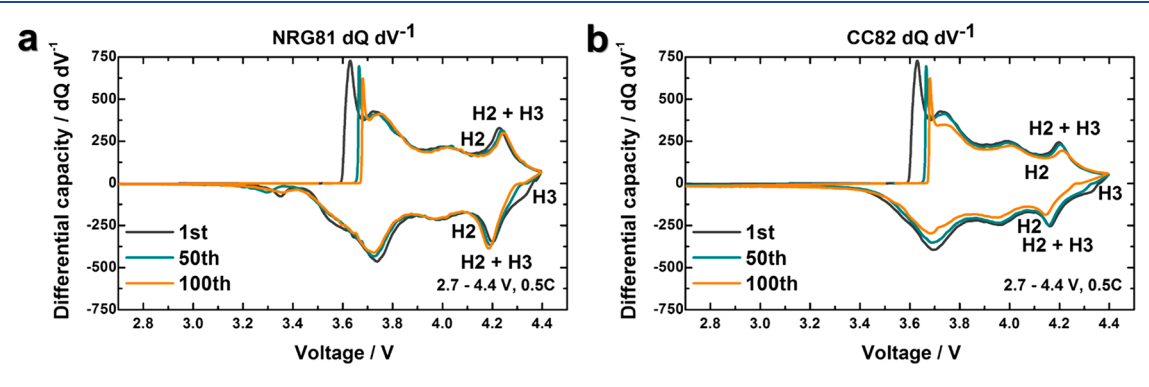


Figure 5. The 1st, 50th, and 100th dQ dV⁻¹ profiles of (a) NRG81 and (b) CC82. The H2 \rightarrow H3 phase transition is labeled.

delineate the impact of the volume change during the H2 \rightarrow H3 phase transformation on the cathode microstructure, cathode particles at 1st cycle charged states of 4.2 and 4.4 V were cut open with a cross-polisher and observed under SEM (Figure 4c-f). The two voltages were chosen because the former is the apex of the $H2 \rightarrow H3$ transformation, as indicated by $dQ dV^{-1}$ curves (Figure 5), and the latter is the cutoff voltage. As seen in the cross-section SEM images of Figure 4, cracks in the microstructure occurred for both NRG81 and CC82, but whereas they are confined to the bulk in NRG81 with no noticeable differences between 4.2 and 4.4 V charged NRG81 particles, the cracks propagated in CC82

with exacerbated crack propagation in the 4.4 V charged CC82 electrode. After multiple repeated lattice parameter/volume changes (20th cycle), NRG81 displayed the same parameter and volume changes, but CC82 showed considerably decreased changes to $\Delta a = -2.08\%$, $\Delta c = -3.39\%$, and ΔV = -5.10% compared to its original $\Delta a = -2.08\%$, $\Delta c =$ -3.56%, and $\Delta V = -5.38\%$ (Figure 4a,b). Note that the ~5% irreversible loss of lithium (3.4% for NRG81 and 7.0% for CC82) can be ascribed to the surface transformation to cathode electrode interface (CEI) formation. 13,16 It appears that the NRG81 microstructure, despite its larger ΔV than ΔV of CC82 resulting from more lithium extraction, can expand

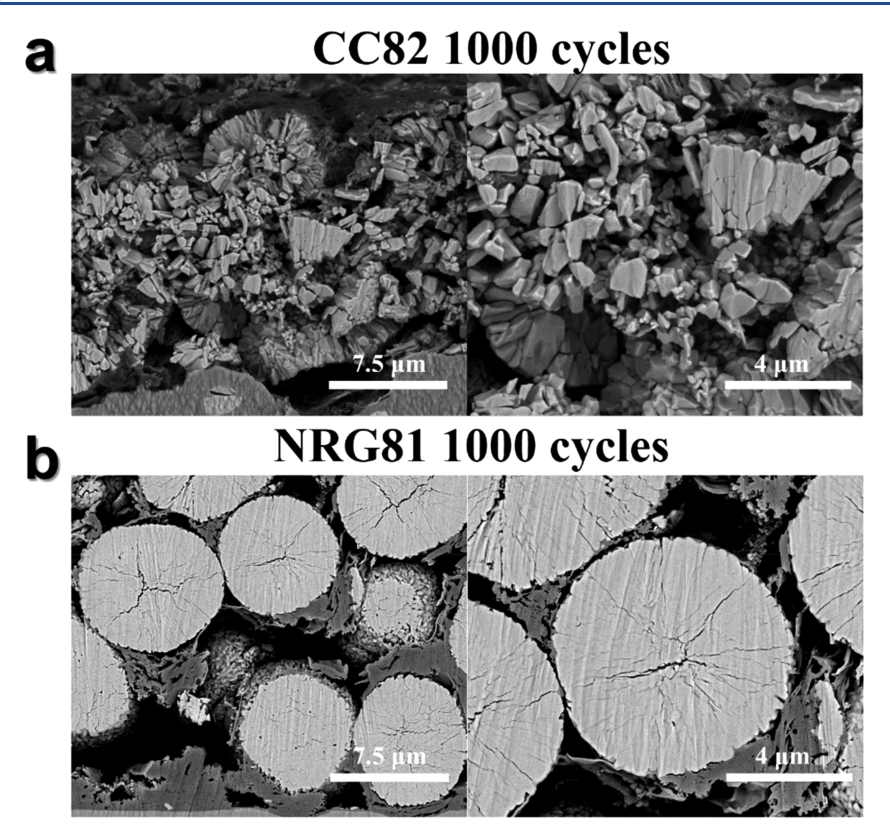


Figure 6. Cross-sectioned SEM images of discharged state (a) CC82 and (b) NRG81 after 1000 cycles.

and contract reversibly (same 1st and 20th cycle ΔV) due to the presence of the radially arranged elongated nanorods in the shell. The radially columnar orientation of the nanorods allows them to act as buffers to mitigate the stress arising from the highly Ni-rich bulk during the H2 \rightarrow H3 transition by uniformly dispersing mechanical stress to reduce stress accumulation. Furthermore, the compact packing of the nanorods confines the cracks to the bulk and suppresses crack propagation from reaching the surface, thus obstructing electrolyte penetration into the reactive Ni-rich core. Consequently, the H2 → H3 phase transition peak in the NRG81 dQ dV^{-1} profile (Figure 5a) appears reversibly with no significant peak diminishment from the 1st to 100th cycle. In contrast, the anisotropic lattice change by randomly oriented polygonal primary particles of CC82 results in irreversible microstructure damage through stress accumulation and cracking along the grain boundaries and results in gradual weakening of the CC82 dQ dV $^{-1}$ H2 \rightarrow H3 phase transition peak as seen in Figure 5b. The culmination of such repeated anisotropic lattice change after 1000 cycles results in complete disintegration of CC82 secondary particles into individual primary particles, whereas the nanorod structured NRG81 maintained its particle cohesion as seen in Figure 6.

3.5. Nanostructure Preservation. To further understand the structural integrity of the nanorod gradient cathode material, a cross-sectioned particle sample was fabricated from the post-mortem NRG81 full-cell with a focused ion beam (FIB), and TEM analysis was performed to verify the nanostructure preservation (Figure 7). In particular, microcracks in the bulk and the adjacent areas have been observed with high-resolution TEM (HR-TEM) to check for structural changes. Because of repeated (1000 times) strenuous anisotropic volume expansion/contraction, cracks had devel-

oped in the highly Ni-rich core. However, its propagation to the surface was suppressed by the radially elongated rodshaped primary particles in the shell region. This is important because cracks reaching the surface act as channels for electrolyte infiltration into the highly reactive Ni-rich particle interior, ¹⁶ and exposure to infiltrated electrolyte results in rapid structure degradation. One such channel is shown in Figure 7b (circled in yellow in Figure 7a) and is ~3 nm wide. As electrolyte was prevented from passing through the microcrack, the layered-to-rock-salt (NiO) nanostructure phase transformation along the crack boundaries did not occur. Indeed, a selected area electron diffraction (SAED) image of the bulk particles adjacent to the cracks in the inset of Figure 7c reflects a distinct layered pattern. Furthermore, the zoomedin HR-TEM image of the circled region in Figure 7c, as shown in Figure 7d, revealed that the layered structure was well maintained and the Fourier transform images of three regions (regions I, II, and III) near the particle surface in Figure 7d clearly exhibit diffraction patterns matching the layered phase of the interior (region IV). This preservation of the layered nanostructure in the bulk attests to the structural stability of the NRG81 cathode as the suppression of the interparticle crack propagation by the surface nanorod structure in the particle outer shell region protected the Ni-rich particle core from electrolyte exposure, thus preventing evolution of the electrically insulating rock-salt phase along the interparticle crack network. Figure 7e shows a typical surface structure of the NRG81 cathode after extensive cycling (1000 cycles). Inevitably, a NiO-like rock-salt surface layer developed due to exposure to electrolyte, and this is often observed in cycled Nirich NCM cathodes and causes an increase in impedance; the slight voltage fade NRG81 experienced, as seen in Figure 3c, can also be attributed to electrolyte exposure. Still, even after

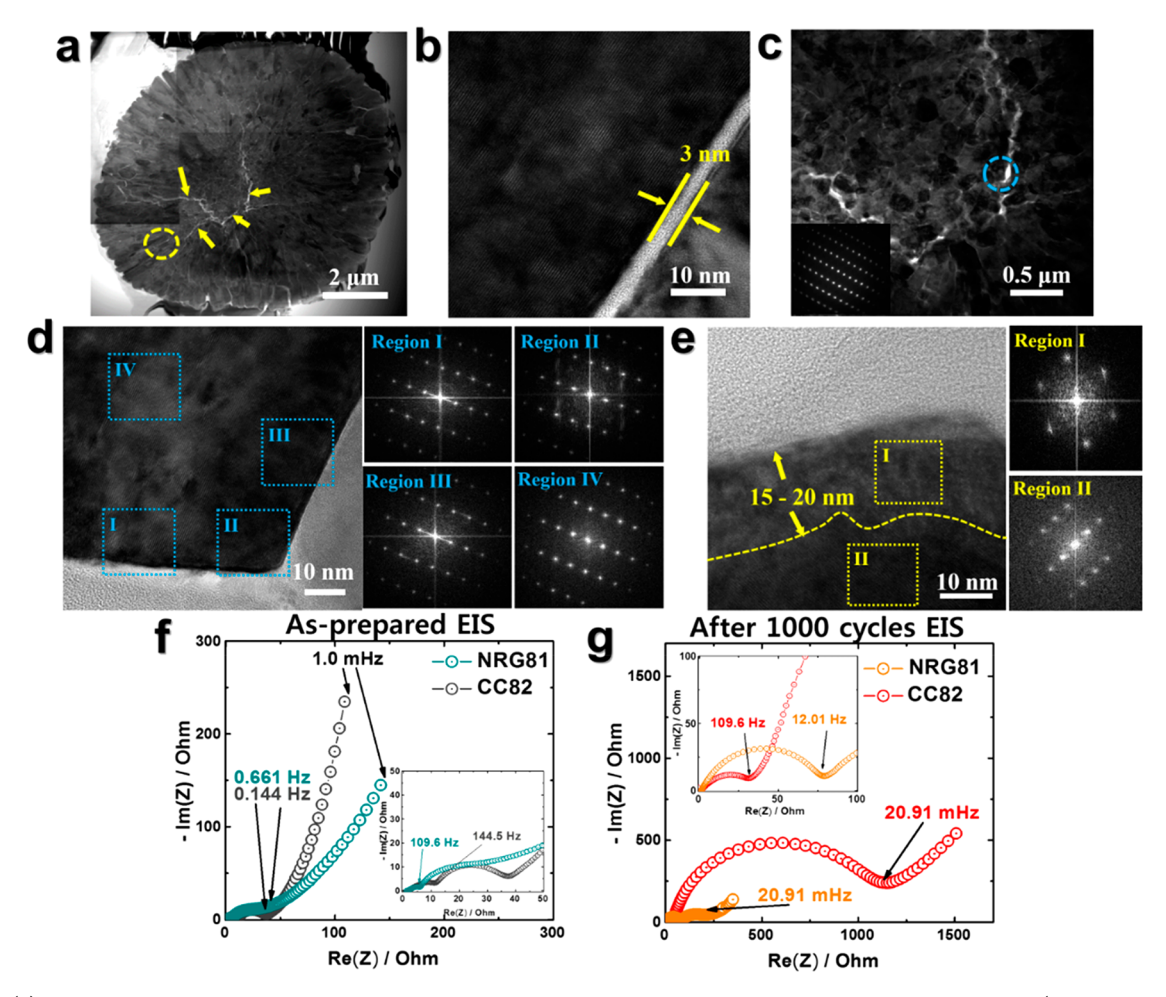


Figure 7. (a) Bright-field scanning TEM cross-sectional image of the cycled NRG81 cathode particle after 1000 cycles (yellow arrows indicate cracks in the macrostructure). (b) High-resolution TEM (HR-TEM) image of the circled region in (a) showing the width of a crack. (c) TEM image of the bulk and its corresponding SAED image. (d) Particle bulk HR-TEM image of the circled region in (c) and Fourier transform images of the regions I, II, III, and IV. (e) HR-TEM image of particle surface and corresponding Fourier transform images of the regions I and II. EIS curves of (f) as-prepared NRG81 and CC82 and (g) after 1000 cycles.

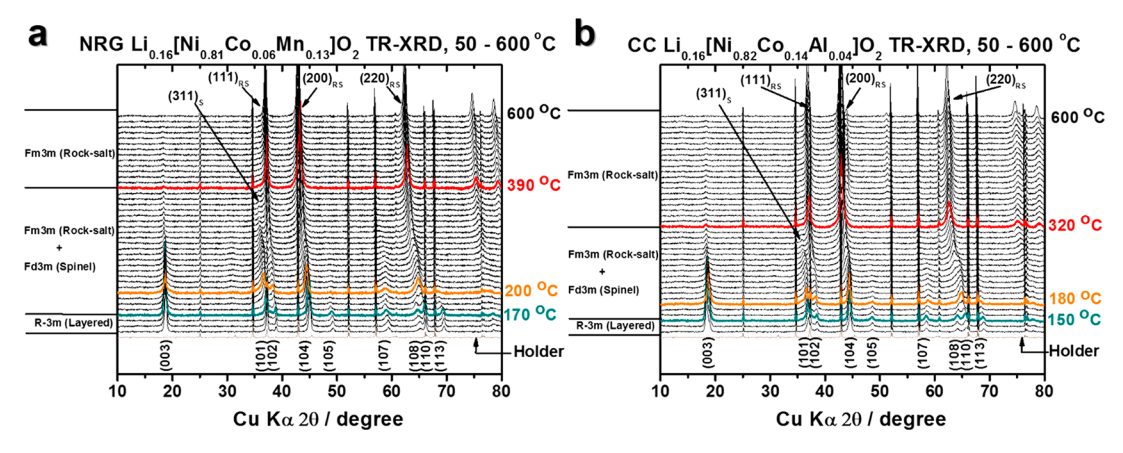


Figure 8. Time-resolved XRD patterns of overcharged (a) NRG81 Li_{0.16}[Ni_{0.81}Co_{0.06}Mn_{0.13}]O₂ and (b) CC82 Li_{0.16}[Ni_{0.82}Co_{0.14}Al_{0.04}]O₂ in the absence of electrolyte. Layered to spinel transition start and finish patterns are colored in cyan and orange, respectively, and the spinel to rock-salt pattern is colored in red.

1000 cycles, the NiO-like surface layer is limited to 15-20 nm in thickness due to positioning of the more chemically stable Mn in the nanorod particle exterior. In comparison, the CC82 cathode without the nanorod structure of the NRG81 cathode sustained severe structural and chemical damage which

eventually pulverized the cathode and exposed individual primary particles to electrolyte attack. Consequently, as seen in Figure 7f,g, whereas the charge transfer resistance (R_{ct}) of NRG81 increased from 29.55 Ω (as-prepared cell) to 133.83 Ω (after 1000 cycles cell), the R_{ct} of CC82 dramatically escalated

from 26.6 Ω (as-prepared cell) to 1112.47 Ω (1000 cycles cell). As such, the nanorod gradient Li[Ni_{0.81}Co_{0.06}Mn_{0.13}]O₂ circumvents the degradation mechanism¹⁶ that plagues conventional constant concentration Ni-rich cathodes through its functional nanorods and testifies to the successful engineering of the NRG81 cathode.

3.6. Thermal Stability. Even under the strenuous conditions of a high-temperature lithium-deficient state, where the cathode structure is susceptible to conversion to more stable phases, NRG81 exhibits better thermal microstructure stability. Figure 8 shows a series of time-resolved XRD (TR-XRD) patterns of overcharged NRG81 Li_{0.16} [Ni_{0.81}Co_{0.06}Mn_{0.13}]O₂ and CC82 $Li_{0.16}[Ni_{0.82}Co_{0.14}Al_{0.04}]O_2$ measured from 50 to 600 °C in the absence of electrolyte. The phase transition from layered (Rm) to M_3O_4 -type (M = transition metal) disordered spinel (Fdm) started at 170 and 150 °C for NRG81 and CC82 (highlighted in cyan), respectively, as evidenced by a decrease in peak intensity of (003)_R and completed at 200 and 180 °C with the merging of the $(108)_R$ and $(110)_R$ peaks.^{44–46} Concurrently, the $(003)_R/(104)_R$ peak ratio significantly decreased, further suggesting transition metal migration. Note that because of the overcharged layered oxide state, the transition from layered to M₃O₄-type spinel occurred rapidly, showing direct transitions between the two phases without formation of a LiMn₂O₄-type spinel. 44,45 With further temperature increase, the spinel phase gradually changed irreversibly into the rock-salt phase (Fmm) as indicated by the (311)_s peak intensity decrease. This second phase transition leads to more oxygen release than the first phase transition and is a serious safety concern for LIBs. Yang et al. 46 suggested via in situ TEM that the phase transition from layered to spinel to rock-salt propagates gradually from particle exterior to interior and the presence of Mn on the surface suppresses transformation to the rock-salt structure. Likewise, while most of the spinel phase transformed into a rock-salt phase (highlighted in red) by 320 °C for CC82, the NRG81 rock-salt transformation occurred at the considerably delayed temperature of 390 °C due to its concentration graded nanorods which concentrates Mn in the rod exterior.

4. CONCLUSION

In conclusion, a specifically designed, layered cathode material was developed to address the need for a high energy density and cycling performance cathode. The NRG81 material has a highly Ni-rich core and graded columnar nanorods that are arranged radially and delivers 225 mAh g⁻¹ (~830 Wh kg⁻¹) with 91% capacity retention (100 cycles) in half-cells and 88% capacity retention (1000 cycles) in full-cells. The high energy density of the NRG81 cathode comes from its highly Ni-rich core, which in turn exacerbates volume change caused by the $H2 \rightarrow H3$ phase transition. Fortunately, the radial nanorods in the particle exterior act as buffers to dissipate the stress arising from the H2 \rightarrow H3 phase transition and suppress the crack network from propagating to the surface to maintain particle coherency. This prevents subsequent electrolyte infiltration via interparticle cracks and rock-salt impurity phase (NiO) transformation along the crack network as evidenced by the HR-TEM image of the cathode particle cross section. As such, the layered nanostructure in the high capacity but reactive Nirich core is preserved, allowing the nanorod gradient cathode to continuously deliver high specific discharge capacities during long-term cycling.

ASSOCIATED CONTENT

Supporting Information

The Supporting Information is available free of charge on the ACS Publications website at DOI: 10.1021/acsaem.9b01116.

NRG81 precursor Ni, Co, and Mn EPMA concentrations and SEM image, CC82 SEM image, NRG81 and CC82 Rietveld refined XRD patterns, NRG81 vs CC82 rate capability performance, NRG81 and CC82 1st and 20th in situ XRD contour plots (PDF)

AUTHOR INFORMATION

Corresponding Author

*E-mail: mullins@che.utexas.edu (C.B.M.).

Adam Heller: 0000-0003-0181-1246 C. Buddie Mullins: 0000-0003-1030-4801

Notes

The authors declare no competing financial interest.

ACKNOWLEDGMENTS

The authors gratefully acknowledge support from the Welch Foundation via Grants F-1131 (A.H.) and F-1436 (C.B.M.) and also the National Science Foundation through Grant CBET-1603491. The authors also thank Yang-Kook Sun and Chong S. Yoon at Hanyang University for providing the hydroxide precursors for the NRG81 samples and the assistance with TEM, respectively.

REFERENCES

- (1) Mizushima, K.; Jones, P. C.; Wiseman, P. J.; Goodenough, J. B. $\text{Li}_{x}\text{CoO}_{2}$ (0 < x < 1): A New Cathode Material for Batteries of High Energy Density. Mater. Res. Bull. 1980, 15, 783-789.
- (2) Yang, S. F.; Zavalij, P. Y.; Whittingham, M. S. Hydrothermal Synthesis of Lithium Iron Phosphate Cathodes. Electrochem. Commun. **2001**, 3, 505-508.
- (3) Gummow, R. J.; de Kock, A.; Thackeray, M. M. Improved Capacity Retention in Rechargeable 4 V Lithium/Lithium-Manganese Oxide (Spinel) Cells. Solid State Ionics 1994, 69, 59-67.
- (4) Arai, H.; Okada, S.; Ohtsuka, H.; Ichimura, M.; Yamaki, J. Characterization and Cathode Performance of Li_{1-X}Ni_{1+X}O₂ Prepared with the Excess Lithium Method. Solid State Ionics 1995, 80, 261-
- (5) Kim, J. H.; Myung, S. T.; Yoon, C. S.; Kang, S. G.; Sun, Y.-K. Comparative Study of LiNi_{0.5}Mn_{1.5}O_{4. δ} and LiNi_{0.5}Mn_{1.5}O₄ Cathodes Having Two Crystallographic Structures: Fd3 m and P4332. Chem. Mater. 2004, 16, 906-914.
- (6) Lin, J.; Lim, J. M.; Youn, D. H.; Kawashima, K.; Kim, J. H.; Liu, Y.; Guo, H.; Henkelman, G.; Heller, A.; Mullins, C. B. Self-Assembled Cu-Sn-S Nanotubes with High (De)Lithiation Performance. ACS Nano 2017, 11 (10), 10347-10356.
- (7) Abel, P. R.; Chockla, A. M.; Lin, Y. M.; Holmberg, V. C.; Harris, J. T.; Korgel, B. A.; Heller, A.; Mullins, C. B. Nanostructured Si_(1-x)Ge_x for Tunable Thin Film Lithium-Ion Battery Anodes. ACS Nano 2013, 7, 2249-2257.
- (8) Youn, D. H.; Stauffer, S. K.; Xiao, P.; Park, H.; Nam, Y.; Dolocan, A.; Henkelman, G.; Heller, A.; Mullins, C. B. Simple Synthesis of Nanocrystalline Tin Sulfide/N-Doped Reduced Graphene Oxide Composites as Lithium Ion Battery Anodes. ACS Nano 2016, 10 (12), 10778-10788.
- (9) Lee, M. H.; Kang, Y. J.; Myung, S. T.; Sun, Y.-K. Synthetic Optimization of $Li[Ni_{1/3}Co_{1/3}Mn_{1/3}]O_2$ via Co-Precipitation. Electrochim. Acta 2004, 50, 939-948.
- (10) Myung, S. T.; Maglia, F.; Park, K. J.; Yoon, C. S.; Lamp, P.; Kim, S. J.; Sun, Y.-K. Nickel-Rich Layered Cathode Materials for

- Automotive Lithium-Ion Batteries: Achievements and Perspectives. ACS Energy Lett. 2017, 2, 196-223.
- (11) Sun, H. H.; Choi, W.; Lee, J. K.; Oh, I. H.; Jung, H. G. Control of Electrochemical Properties of Nickel-Rich Layered Cathode Materials for Lithium Ion Batteries by Variation of the Manganese to Cobalt Ratio. J. Power Sources 2015, 275, 877-883.
- (12) Watanabe, S.; Kinoshita, M.; Hosokawa, T.; Morigaki, K.; Nakura, K. Capacity Fade of LiAl_vNi_{1-x-v}Co_xO₂ Cathode for Lithium-Ion Batteries during Accelerated Calendar and Cycle Life Tests (Surface Analysis of LiAl_vNi_{1-x-v}Co_xO₂ Cathode after Cycle Tests in Restricted Depth of Discharge Ranges). J. Power Sources 2014, 258, 210-217.
- (13) Liu, H.; Wolf, M.; Karki, K.; Yu, Y. S.; Stach, E. A.; Cabana, J.; Chapman, K. W.; Chupas, P. J. Intergranular Cracking as a Major Cause of Long-Term Capacity Fading of Layered Cathodes. Nano Lett. 2017, 17, 3452-3457.
- (14) U.S. Department of Energy. 2015 Annual Progress Report for Energy Storage R&D 2016, 1 (2), 11.
- (15) Noh, H. J.; Youn, S.; Yoon, C. S.; Sun, Y.-K. Comparison of the Structural and Electrochemical Properties of Layered Li[Ni, Co, Mn,]- O_2 (x = 1/3, 0.5, 0.6, 0.7, 0.8 and 0.85) Cathode Material for Lithium-Ion Batteries. J. Power Sources 2013, 233, 121-130.
- (16) Ryu, H. H.; Park, K. J.; Yoon, C. S.; Sun, Y.-K. Capacity Fading of Ni-Rich Li[Ni_xCo_yMn_{1-x-y}]O₂ (0.6 $\leq x \leq$ 0.95) Cathodes for High-Energy-Density Lithium-Ion Batteries: Bulk or Surface Degradation? Chem. Mater. 2018, 30, 1155-1163.
- (17) Chen, Z.; Qin, Y.; Amine, K.; Sun, Y.-K. Role of Surface Coating on Cathode Materials for Lithium-Ion Batteries. J. Mater. Chem. 2010, 20, 7606-7612.
- (18) Lee, J. H.; Yoon, C. S.; Hwang, J.-Y.; Kim, S.-J.; Maglia, F.; Lamp, P.; Myung, S.-T.; Sun, Y.-K. High-Energy-Density Lithium-Ion Battery Using a Carbon-Nanotube-Si Composite Anode and a Compositionally Graded $Li[Ni_{0.85}Co_{0.05}Mn_{0.10}]O_2$ Cathode. Energy Environ. Sci. 2016, 9, 2152-2158.
- (19) Yoon, C. S.; Kim, U.-H.; Park, G.-T.; Kim, S. J.; Kim, K.-H.; Kim, J.; Sun, Y.-K. Self-Passivation of a LiNiO2 Cathode for a Lithium-Ion Battery through Zr Doping. ACS Energy Lett. 2018, 3, 1634-1639.
- (20) Zheng, S.; Huang, R.; Makimura, Y.; Ukyo, Y.; Fisher, C. A. J.; Hirayama, T.; Ikuhara, Y. Microstructural Changes in Li-Ni_{0.8}Co_{0.15}Al_{0.05}O₂ Positive Electrode Material during the First Cycle. J. Electrochem. Soc. 2011, 158, A357-A362.
- (21) Ohzuku, T. Electrochemistry and Structural Chemistry of LiNiO (R3 m) for 4 V Secondary Lithium Cells. J. Electrochem. Soc. 1993, 140, 1862-1870.
- (22) Miller, D. J.; Proff, C.; Wen, J. G.; Abraham, D. P.; Bareño, J. Observation of Microstructural Evolution in Li Battery Cathode Oxide Particles by In Situ Electron Microscopy. Adv. Energy Mater. 2013, 3, 1098-1103.
- (23) Yoon, C. S.; Jun, D.-W.; Myung, S.-T.; Sun, Y.-K. Structural Stability of LiNiO2 Cycled above 4.2 V. ACS Energy Lett. 2017, 2,
- (24) Kondrakov, A. O.; Schmidt, A.; Xu, J.; Geßwein, H.; Mönig, R.; Hartmann, P.; Sommer, H.; Brezesinski, T.; Janek, J. Anisotropic Lattice Strain and Mechanical Degradation of High-and Low-Nickel NCM Cathode Materials for Li-Ion Batteries. J. Phys. Chem. C 2017, 121, 3286-3294.
- (25) Reimers, J. N.; Rossen, E.; Jones, C. D.; Dahn, J. R. Structure and Electrochemistry of LixFe, Ni1-YO2. Solid State Ionics 1993, 61, 335 - 344.
- (26) Pouillerie, C.; Croguennec, L.; Delmas, C. $\text{Li}_x \text{Ni}_{1-y} \text{Mg}_y \text{O}_2$ (y = 0.05, 0.10) System: Structural Modifications Observed upon Cycling. Solid State Ionics 2000, 132, 15-29.
- (27) Subramanian, V.; Fey, G. T. K. Preparation and Characterization of $LiNi_{0.7}Co_{0.2}Ti_{0.05}M_{0.05}O_2$ (M = Mg, Al and Zn) Systems as Cathode Materials for Lithium Batteries. Solid State Ionics 2002, 148, 351-358.

- (28) Wilcox, J.; Patoux, S.; Doeff, M. Structure and Electrochemistry of $LiNi_{1/3}Co_{1/3-y}M_yMn_yO_2$ (M = Ti, Al, Fe) Positive Electrode Materials. J. Electrochem. Soc. 2009, 156, A192-A198.
- (29) Park, K.-J.; Jung, H.-G.; Kuo, L.-Y.; Kaghazchi, P.; Yoon, C. S.; Sun. Y.-K. Improved Cycling Stability of Li[Ni_{0.90}Co_{0.05}Mn_{0.05}]O₂ Through Microstructure Modification by Boron Doping for Li-Ion Batteries. Adv. Energy Mater. 2018, 8, 1801202.
- (30) Kim, U.-H.; Jun, D.-W.; Park, K.-J.; Zhang, Q.; Kaghazchi, P.; Aurbach, D.; Major, D. T.; Goobes, G.; Dixit, M.; Leifer, N.; Wang, C.; Yan, P.; Ahn, D.; Kim, K.-H.; Yoon, C. S.; Sun, Y.-K. Pushing the Limit of Layered Transition Metal Oxide Cathodes for High-Energy Density Rechargeable Li Ion Batteries. Energy Environ. Sci. 2018, 11,
- (31) Chen, Z.; Dahn, J. R. Reducing Carbon in LiFePO₄/C Composite Electrodes to Maximize Specific Energy, Volumetric Energy, and Tap Density. J. Electrochem. Soc. 2002, 149, A1184-A1189.
- (32) Myung, S. T.; Izumi, K.; Komaba, S.; Sun, Y.-K.; Yashiro, H.; Kumagai, N. Role of Alumina Coating on Li-Ni-Co-Mn-O Particles as Positive Electrode Material for Lithium-Ion Batteries. Chem. Mater. **2005**, 17, 3695-3704.
- (33) Jang, S. B.; Kang, S. H.; Amine, K.; Bae, Y. C.; Sun, Y.-K. Synthesis and Improved Electrochemical Performance of Al(OH)3-Coated Li[Ni_{1/3}Mn_{1/3}Co_{1/3}]O₂ Cathode Materials at Elevated Temperature. Electrochim. Acta 2005, 50, 4168-4173.
- (34) Sun, Y.-K.; Han, J. M.; Myung, S. T.; Lee, S. W.; Amine, K. Significant Improvement of High Voltage Cycling Behavior AlF₃-Coated LiCoO₂ Cathode. Electrochem. Commun. 2006, 8, 821-826.
- (35) Takamatsu, D.; Mori, S.; Orikasa, Y.; Nakatsutsumi, T.; Koyama, Y.; Tanida, H.; Arai, H.; Uchimoto, Y.; Ogumi, Z. Effects of ZrO₂ Coating on LiCoO₂ Thin-Film Electrode Studied by In Situ X-Ray Absorption Spectroscopy. J. Electrochem. Soc. 2013, 160, A3054-A3060.
- (36) Sun, Y.-K.; Myung, S. T.; Park, B. C.; Prakash, J.; Belharouak, I.; Amine, K. High-Energy Cathode Material for Long-Life and Safe Lithium Batteries. Nat. Mater. 2009, 8, 320-324.
- (37) Sun, Y.-K.; Chen, Z.; Noh, H. J.; Lee, D. J.; Jung, H. G.; Ren, Y.; Wang, S.; Yoon, C. S.; Myung, S. T.; Amine, K. Nanostructured High-Energy Cathode Materials for Advanced Lithium Batteries. Nat. Mater. 2012, 11, 942-947.
- (38) Lim, B. B.; Yoon, S. J.; Park, K. J.; Yoon, C. S.; Kim, S. J.; Lee, J. J.; Sun, Y.-K. Advanced Concentration Gradient Cathode Material with Two-Slope for High-Energy and Safe Lithium Batteries. Adv. Funct. Mater. 2015, 25, 4673-4680.
- (39) Kim, U.-H.; Myung, S.-T.; Yoon, C. S.; Sun, Y.-K. Extending the Battery Life Using an Al-Doped Li[Ni_{0.76}Co_{0.09}Mn_{0.15}]O₂ Cathode with Concentration Gradients for Lithium Ion Batteries. ACS Energy Lett. 2017, 2, 1848-1854.
- (40) Kim, U. H.; Lee, E. J.; Yoon, C. S.; Myung, S. T.; Sun, Y.-K. Compositionally Graded Cathode Material with Long-Term Cycling Stability for Electric Vehicles Application. Adv. Energy Mater. 2016, 6 (22), 1601417.
- (41) Yoon, C. S.; Park, K. J.; Kim, U. H.; Kang, K. H.; Ryu, H. H.; Sun, Y.-K. High-Energy Ni-Rich Li[Ni_xCo_yMn_{1-x-y}]O₂ Cathodes via Compositional Partitioning for Next-Generation Electric Vehicles. Chem. Mater. 2017, 29, 10436-10445.
- (42) Sun, Y.-K.; Myung, S.-T.; Kim, M.-H.; Prakash, J.; Amine, K. Synthesis and Characterization of Li- $[(Ni_{0.8}Co_{0.1}Mn_{0.1})_{0.8}(Ni_{0.5}Mn_{0.5})_{0.2}]O_2$ with the Microscale Core-Shell Structure as the Positive Electrode Material. J. Am. Chem. Soc. **2005**, 127, 13411–13418.
- (43) EcoPro; http://www.ecopro.co.kr/eng (accessed Nov 11, 2018).
- (44) Wu, L.; Nam, K.-W.; Wang, X.; Zhou, Y.; Zheng, J.-C.; Yang, X.-Q.; Zhu, Y. Structural Origin of Overcharge-Induced Thermal Instability of Ni-Containing Layered-Cathodes for High-Energy-Density Lithium Batteries. Chem. Mater. 2011, 23, 3953-3960.
- (45) Bak, S.; Hu, E.; Zhou, Y.; Yu, X.; Senanayake, S. D.; Cho, S.; Kim, K.; Chung, K. Y.; Yang, X.; Nam, K. Structural Changes and

Thermal Stability of Charged LiNi_xMn_yCo_zO₂ Cathode Materials Studied by Combined *In Situ* Time-Resolved XRD and Mass Spectrocopy. *ACS Appl. Mater. Interfaces* **2014**, *6*, 22594–22601. (46) Nam, K.-W.; Bak, S.-M.; Hu, E.; Yu, X.; Zhou, Y.; Wang, X.; Wu, L.; Zhu, Y.; Chung, K.-Y.; Yang, X.-Q. Combining *in situ* Synchrotron X-Ray Diffraction and Absorption Techniques with Transmission Electron Microscopy to Study the Origin of Thermal Instability in Overcharged Cathode Materials for Lithium-Ion Batteries. *Adv. Funct. Mater.* **2013**, 23, 1047–1063.